The role of hydrogen molecular effects on detachment in Magnum-PSI

G.R.A. Akkermans[1*], I.G.J. Classen[1], R. Perillo[2], H.J. van der Meiden[1], F. Federici[3], S. Brezinsek[4], and the Magnum-PSI team[1].

[1] *DIFFER Dutch Institute for Fundamental Energy Research, De Zaale 20, 5612AJ, Eindhoven, the Netherlands*
[2] *University of California San Diego, 9500 Gilman Dr, La Jolla, CA 92093, USA*
[3] *Department of Physics, University of York, Heslington, York, YO10 5DD, UK*
[4] *Forschungszentrum Jülich GmbH, Institut für Energie und Klimaforschung, 52425 Jülich, Germany*
[*] *Corresponding author: g.r.a.akkermans@differ.nl*

Abstract

The hydrogen plasma-chemical processes responsible for tokamak divertor detachment are studied experimentally in the linear device Magnum-PSI, with a focus on Molecular Activated Recombination (MAR) in hydrogen plasmas. Hydrogen plasmas with electron densities up to $6 \cdot 10^{20}\ \mathrm{m}^{-3}$ were created in Magnum-PSI and hydrogen gas puffing was used to locally enhance plasma-neutral interaction. Thomson Scattering and Balmer line spectroscopy measurements show that as neutral pressure is increased, the plasma passes through regimes dominated by ionization, MAR, and electron ion recombination (EIR) in turn. Heat and particle fluxes decrease monotonically with pressure. Fulcher band measurements show that in our plasma conditions, a simple model based on Franck-Condon excitation of a thermal vibrational distribution fails to describe the vibrational distribution of the upper state. These results serve as a benchmark for modelling suites that aim to simulate the ITER divertor, and motivates their accurate treatment of the discussed processes, particularly MAR.

Introduction

In ITER and other next-generation devices confining fusion-grade deuterium-tritium plasmas, operating in a detached or semi-detached divertor regime will likely be mandatory in order to limit heat loads to plasma-facing components (PFCs) to the tungsten material limit of $10\ \frac{\mathrm{MW}}{\mathrm{m}^2}$ [1]. Divertor detachment has been achieved in many tokamak experiments [2, 3, 4, 5] and is characterized by an interplay of plasma-neutral processes which lead to a plasma pressure loss along the field line, and ultimately to a reduction in heat and particle fluxes to PFCs [6].

As some examples of relevant processes in detachment, radiation from seeded impurities directly distributes heat and decreases the electron temperature. Elastic collisions and resonant charge-exchange between plasma main ions and hydrogenic neutrals transfers energy and momentum to particles not confined by the magnetic field, resulting in power spreading and a decrease in ion temperature and flow speed. Finally, volume recombination produces excited hydrogen (deuterium, tritium). If this decays to the ground state rather than being re-ionized, it reduces the particle flux and hence the amount of ion-electron pairs that deposit their ionization energy while recombining on the PFC surface.

The candidate processes leading to volume recombination are atomic electron-ion recombination (EIR) – which occurs either radiatively or as a three-body reaction – and molecular activated recombination (MAR). We consider MAR in hydrogen plasma in this work, noting that there are considerable differences in rates for the deuterium and tritium isotopes. The MAR reaction has two branches, each of them a two-step process. The first branch, mediated by the molecular ion H_2^+, consists of ion conversion followed by dissociative recombination:

$$H_2^v + H^+ \rightarrow H_2^+ + H, \qquad H_2^+ + e^- \rightarrow H^* + H \tag{1}$$

The second branch includes the negative ion H^- and consists of dissociative attachment followed by mutual recombination:

$$H_2^v + e^- \rightarrow H^- + H, \qquad H^- + H^+ \rightarrow H^* + H \tag{2}$$

In both reactions, H_2^v indicates a vibrationally excited molecule with $v \geq 4$ [7]. In deuterium and tritium, differences in the vibrational energy structure cause large differences in MAR rates.

Other possible MAR pathways exist. For example, proton transfer between H_2^+ and H_2 forms H_3^+, which can undergo dissociative recombination. This H_3^+ branch of MAR is suggested to play an important role in plasma recombination, for example in [8]. However, for electron densities $> 10^{19}$ m^{-3}, as is the case in the ITER divertor and in typical Magnum-PSI plasmas, the H_2^+ lifetime is very short due to efficient dissociative recombination, and barely any H_3^+ is produced [9].

An analysis of the effective rate coefficient of MAR K_{MAR} in hydrogen plasma, accounting for branches (1) and (2), vibrational distribution, and competing reactions for H_2^+ and H^- that do not lead to recombination, found that K_{MAR} reaches a maximum at an electron temperature T_e of around 1 eV [10]. Comparing the values to rate coefficients for EIR and ionization [11], as is done in Figure 1, it is clear that the MAR rate coefficient is larger than that of EIR for $\mathrm{T_e} \gtrsim 0.5$ eV and larger than that of ionization for $\mathrm{T_e} \lesssim 2$ eV. At sufficiently low dissociation rate and ionization degree, this means that the MAR rate $K_{MAR} n_e n_{H_2}$ can dominate over the EIR rate $K_{EIR} n_e n_{H^+}$ and the ionization rate $K_{iz} n_e n_H$ around the aforementioned T_e range.

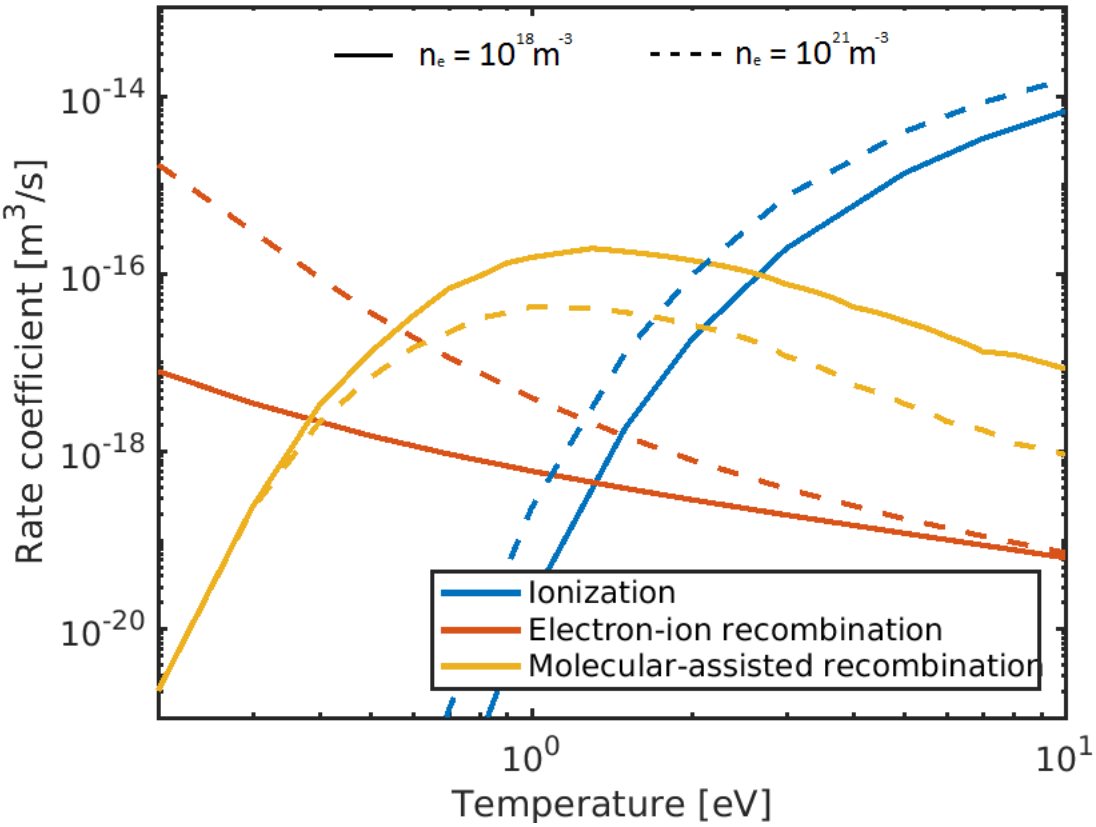

Figure 1: Rate coefficients for hydrogen plasma processes as function of electron temperature for the ionization and recombination reactions. The solid and dotted lines indicate densities of $1 \cdot 10^{18}$ m^{-3} and $1 \cdot 10^{21}$ m^{-3}, respectively. MAR dominates over EIR for $T_e \gtrsim 0.5$ eV and over ionization for $T_e \lesssim 2$ eV.

MAR has been a subject of study in many linear plasma devices, which aim to study plasmas relevant to the tokamak divertor with the advantages of simple geometry, good diagnostic access, and steady-state operation. Many such studies showed that MAR played an important role as a recombing agent in the plasmas studied [12, 13, 14]. In Pilot-PSI, it was observed that MAR took place mostly around the periphery of the narrow plasma beam (d=2-3 cm), due to the molecular density being rarefied further inward. This led to observation of hollow emission profiles of the Balmer β line from H^* produced by MAR mainly at the typical penetration depth of the molecules of 4 mm [15]. The rarefaction of neutrals was not itself caused by MAR but by simple collisional heating of molecules by the background plasma [16].

The MAR reaction is included in the Monte Carlo neutral codes EIRENE [17] and EUNOMIA [18]. EIRENE is part of the SOLPS-ITER code package, in which it is coupled to the multi-fluid code B2.5 describing the charged particles. EUNOMIA-B2.5 is the standard code package used to model Magnum-PSI plasmas. The two neutral codes differ slightly in their technical treatment of MAR, which motivates comparing both codes to experiments in which MAR is observed.

In this work we study the role of MAR and the other processes governing detachment using the linear device Magnum-PSI [19] in hydrogen. Magnum-PSI is unique in its ability to produce plasma temperatures and densities close to those expected in the ITER divertor, in contrast to other linear devices which typically operate at lower densities [20]. Compared to its predecessor Pilot-PSI which was capable of producing similar plasma conditions, Magnum offers steady-state operation at higher magnetization due to the addition of superconducting coils. The addition of a differential pumping scheme allows changes in the downstream neutral pressure without affecting source operation. We use hydrogen gas puffing to investigate different regimes of plasma conditions as well as neutral pressures,

with electron densities n_e between 10^{18} and 10^{21} m^{-3}, T_e between 0.1 and 5 eV, and neutral pressure p_{neut} between 0.2 and 14 Pa. For reference, the plasma at the ITER divertor target is expected to have $T_e = 40 - 1$ eV, $n_e = 5 \cdot 10^{20} - 2 \cdot 10^{21} \mathrm{m}^{-3}$, $p_{neut} = 1.4 - 10.8$ Pa for a power of 100 MW crossing the separatrix, depending on if the divertor is operated in the attached, high-recycling, or semi-detached regime [21].

Experimental set-up and diagnostics

The linear device Magnum-PSI [19] generates plasma using a cascaded arc source, and confines it in an axial magnetic field of up to 2.5 T produced by a superconducting NbTi magnet. The plasma is transported through three chambers, which are differentially pumped to remove neutrals, minimizing plasma losses and neutral influx to the target chamber. An overview of the device is given in Figure 2.

In the experiments presented here, hydrogen gas is injected into hydrogen plasmas from a valve located just behind the target. The neutral background pressure is measured by a baratron type MKS 627B, located further behind the target. The plasma traverses a distance of 0.38 m between the last skimmer and the target.

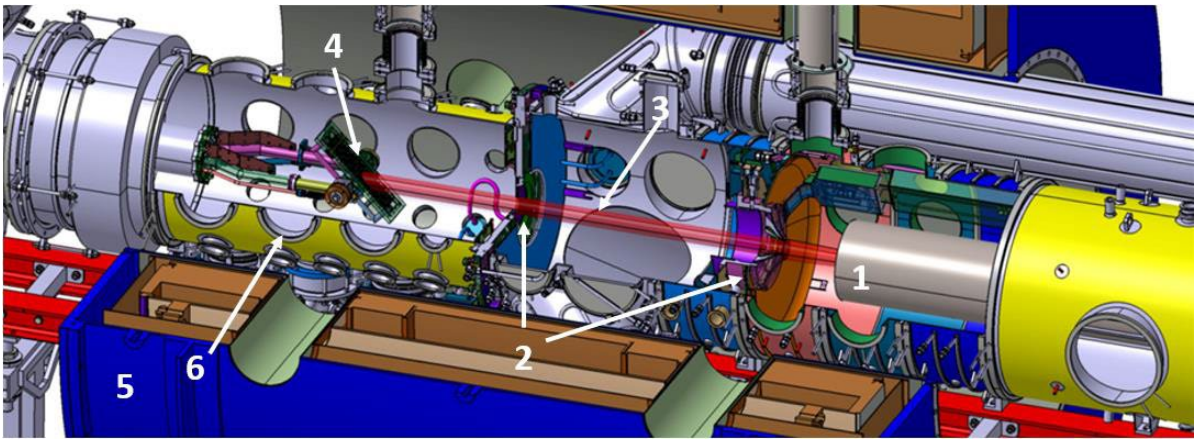

Figure 2: Design of the linear plasma device Magnum-PSI. The numbers correspond to: 1. Plasma source 2. Skimmers separating the three chambers 3. Plasma beam 4. Target 5. Superconducting magnet 6. Gas puff location.

Table 1: Overview of the baseline plasmas studied in this work. All plasmas were created at a magnetic field of 1.2 T and a source hydrogen flow of $2.2 \cdot 10^{21}$ particles/s. Reported are: the plasma source current I_s used; Thomson Scattering results for peak electron temperature $T_{e,peak}$ and density $n_{e,peak}$, and the Full Width at Half Maximum (FWHM) of the n_e profile (characterizing plasma width); and baratron measurements of neutral background pressure p_{neut}.

I_s [A]	$T_{e,peak}$ [eV]	$n_{e,peak}$ [$10^{20}\mathrm{m}^{-3}$]	n_e FWHM [mm]	p_{neut} [Pa]
80	4.4 ± 0.9	0.08 ± 0.01	25	0.155 ± 0.007
140	4.6 ± 0.4	1.2 ± 0.1	12	0.272 ± 0.004
175	2.4 ± 0.2	6.9 ± 0.4	12	0.43 ± 0.01

The target used is a circular tungsten disc 30 mm in diameter and 1 mm thick, mounted perpendicular to the incoming plasma. Profiles of electron temperature T_e and density n_e are measured by a Thomson Scattering (TS) system with a radial resolution of 1.3 mm [22], at a location 25 mm in front of the target. The lower detection limits are 0.05 eV for T_e and $2 \cdot 10^{18}$ m^{-3} for n_e.

Three different 'baseline' plasmas without target chamber gas puffing were created at a constant magnetic field of 1.2 T and hydrogen gas flow through the source of to $2.2 \cdot 10^{21}$ particles/s (5 slm, standard liters per minute), for different values of source current I_S; 80, 140, and 175 A. An overview of the baseline conditions is given in Table 1, and the profiles of T_e and n_e measured by TS are given in Figure 3. The neutral background pressure p_{neut} is in these cases sustained by surface recombination of electron-ion pairs on the target, with little role for neutral transport between the middle and target chambers [19]. Almost two orders of magnitude in peak n_e are covered. Such a strong dependence of n_e on I_S is routinely observed on Magnum-PSI, and may point to significantly improved source efficiency and/or reduced transport losses at high plasma source current operation [19].

Optical Emission Spectroscopy (OES) measurements are taken in the same axial location, using a Jarell-Ash spectrometer of Czerny-Turner design. Two reflecting grating elements are used alternately, one with 150 ln/mm covering a spectral range of 175nm, the other with 2400 ln/mm and a spectral range of 11 nm. Light is relayed to the spectrometer by a linear array of 40 quartz fibers, each 0.4 mm in diameter, and due to the fiber jacket the fiber cores are separated with 50 µm. An achromatic doublet lens (f=10 cm) images the plasma onto this fiber array. The magnification is such that the spatial resolution inside the plasma is about 1.1 mm, i.e., a lateral range of 4.4 cm is covered. Each fiber produces a line-of-sight integrated measurement of the plasma. The OES system is radiometrically calibrated using a Ulbrich-type integration sphere (type: Labsphere USS-800C-035R).

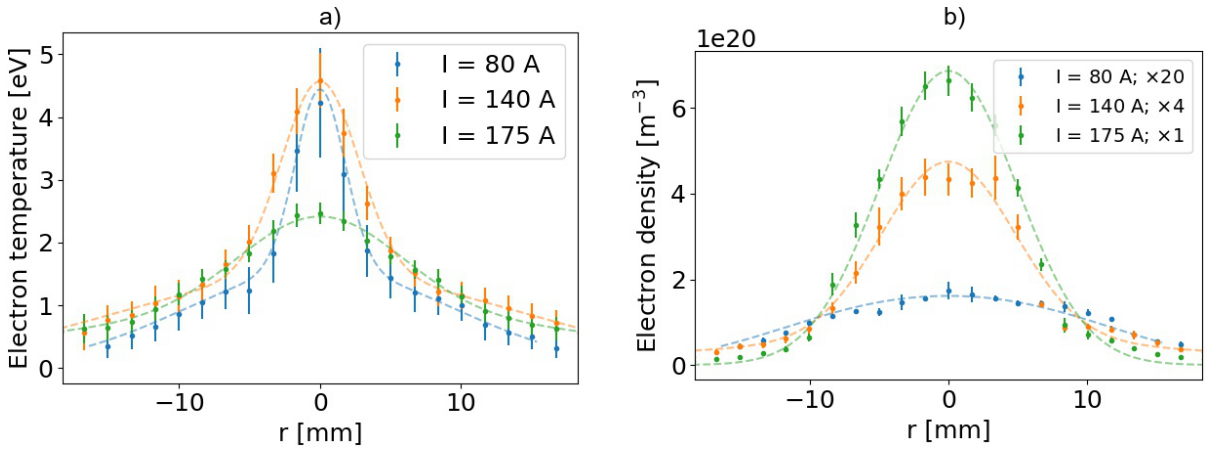

Figure 3: Profiles of electron temperature (a) and density (b) for the three baseline plasma scenarios, i.e., without target chamber gas puffing. Note the scaling factors for the density plot. Error bars indicate reproducibility margin.

Hydrogen gas puff experiments

A variety of divertor-like plasma conditions has been created and studied in Magnum-PSI. At constant plasma source settings, hydrogen gas puffing was used to increase the neutral background pressure p_{neut} to above the baseline level ($0.15 - 0.43$ Pa, see Table 1), enabling the investigation of plasmas with high degrees of plasma-neutral interaction. The peak values of T_e and n_e measured by TS are reported in Figure 4, along with derived values of peak heat and particle flux (explained below).

Figure 4a shows that $T_{e,peak}$ decreases monotonically as a function of p_{neut} due to a gradual increase in volumetric plasma-neutral energy sinks for all values of source current. Figure 4b shows that at 175 A source current, $n_{e,peak}$ also decreases monotonically with p_{neut}, pointing to a gradual increase in the net particle sink. The plasmas at 140 and 80 A show different behavior. Here, at low p_{neut}, $n_{e,peak}$ increases as a function of p_{neut} due to ionization of the extra available neutrals. For gradually increasing pressure, density then peaks, drops, increases and peaks again, and finally decreases to an order of magnitude below that of the baseline plasma.

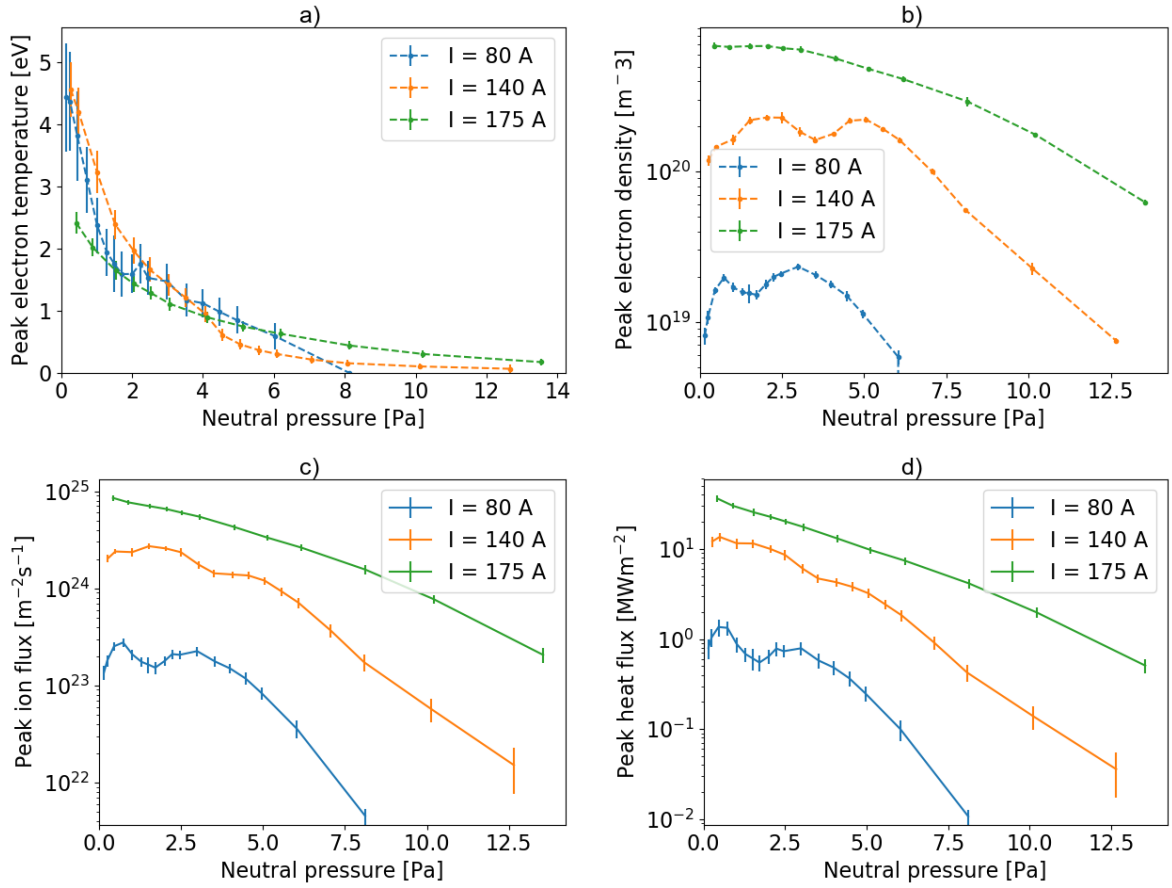

Figure 4: Peak values of electron temperature (a), electron density (b), ion flux (c), and heat flux (d) as a function of neutral background pressure for three different values of plasma source current. The dip in peak density around 2 Pa (80 A, blue) and 4 Pa (140 A, orange) cannot be explained by purely atomic physics and suggests the presence of a molecular particle sink.

Since the rate of atomic ionization decreases and that of recombination increases with decreasing T_e, only one local maximum of $n_{e,peak}$ as function of p_{neut} would be expected if only atomic physics is relevant. Indeed, the extra dip in the two lower-density curves in Figure 4b points to an extra particle sink that is primarily active at moderate p_{neut} and T_e, consistent with the range where MAR is expected to be effective. The fact that no similar dip occurs for the 175 A plasma is likely due to the higher electron density, which leads to a lower relative abundance of neutrals and a decreased relative strength of ionization and MAR compared to EIR.

At first glance, the 80 A results do not seem to quantitatively agree with the theoretical prediction shown in Figure 1. For example, $n_{e,peak}$ has a local maximum at 3.0 Pa (see Figure 4b), indicating that T_e is already too low for MAR to provide a significant particle sink. However, $T_{e,peak} = 1.5$ eV at this same neutral pressure (see Figure 4a) corresponds with the maximum MAR rate in Figure 1. This apparent contradiction is resolved by the sharply peaked nature of the T_e profiles at low source current. Because the molecular density is rarefied in the center of the plasma, the lower T_e near the edge of the beam is what determines the overall MAR rate in the plasma.

The ion flux Γ_i in Figure 4c is calculated from the Bohm flux for adiabatic flow ($\gamma = 5/3$) [23]:

$$\Gamma_i = 0.5 n_e c_s = 0.5 n_e \left(\frac{k_B T_e + \gamma k_B T_i}{m_i}\right)^{1/2}, \quad (3)$$

where we assume a density drop of a factor 2 in the pre-sheath and $T_i = T_e$.

The heat flux q_t arriving at the target, plotted in Figure 4b is calculated as:

$$\begin{aligned} q_t &= \Gamma_i \left(\left(2.5 k_B T_i - e V_s - e V_{ps}\right)\left(1 - R_{i,E}\right) + 2 k_B T_e \left(1 - R_{e,E}\right) + \chi_i + \chi_r (1 - R_n) \right) \quad (4) \\ &= \Gamma_i (5.03 k_B T_e + 14.5 [\mathrm{eV}]), \end{aligned}$$

where the sheath potential drop $V_s = \frac{kT_e}{e} \ln\left(\frac{4c_i}{c_s}\right) = 0.5 \ln\left[\left(2\pi \frac{me}{mi}\right)\left(1 + \frac{\gamma Ti}{Te}\right)\right]$, and the pre-sheath potential drop $V_{ps} = \ln(0.5) \frac{k_B T_e}{e}$. $\chi_i = 13.6$ eV and $\chi_r = 2.2$ eV are the ionization and dissociation energy of hydrogen, and $R_{e,E} = 0.2$, $R_{i,E} = 0.4$, and $R_N = 0.6$ are the energy and neutral reflection coefficients for tungsten [24]. Impact energy dependence of material reflection coefficients and local imbalance between electron and in fluxes compensated around the edge of the beam are neglected.

The results for ion flux more clearly show the difference in behavior of MAR between plasma regimes. For the 80 A plasma, the calculated peak ion flux has a local minimum at ~2 Pa, similar to density. The local dip in Γ_i around 4 Pa is more moderate for the 140 A plasma, since the n_e behavior is partially compensated by the behavior of T_e. The feature is entirely absent in the 175 A plasma. Results for heat flux qualitatively follow those for particle flux, particularly at the higher pressures where $5.03 k_B T_e \ll 14.5$ eV

Atomic spectroscopy

Spatially resolved Optical Emission Spectroscopy of the Balmer series is used to gain further insights about the plasma processes active in the Magnum-PSI plasma by probing excited hydrogen they produce. A low-resolution diffraction grating with 150 ln/mm is used to measure the H_α (corresponding to the $n = 3 \rightarrow n = 2$ transition at 656.3 nm) and H_β (corresponding to the $n = 4 \rightarrow n = 2$ transition at 486.1 nm) lines using one grating angle. Using another grating angle, H_β through to the Balmer continuum at 364.6 nm is measured. A typical measured spectrum is shown in Figure 5. The observed spectral line shape is constant over the measured plasma regimes, due to the instrument function having a width of 2 nm for this coarse grating. Overestimates for other sources of line broadening yield 0.04 nm for Doppler broadening and 0.4 nm for Stark broadening. Hence, measured spectrums are fitted using a constant spectral shape given by the instrument function, and the total radiance of each line is

extracted. Close to the continuum, overlap between the lines is accounted for by fitting all lines at the same time. The fit is performed for data from each fiber, yielding a lateral profile of line radiance as a function of line of sight though the plasma for each spectral line. The 'three-point' numerical Abel inversion method [25] is then applied to these lateral profiles to find the radial profiles of plasma emissivity, which are directly related to the excited state densities.

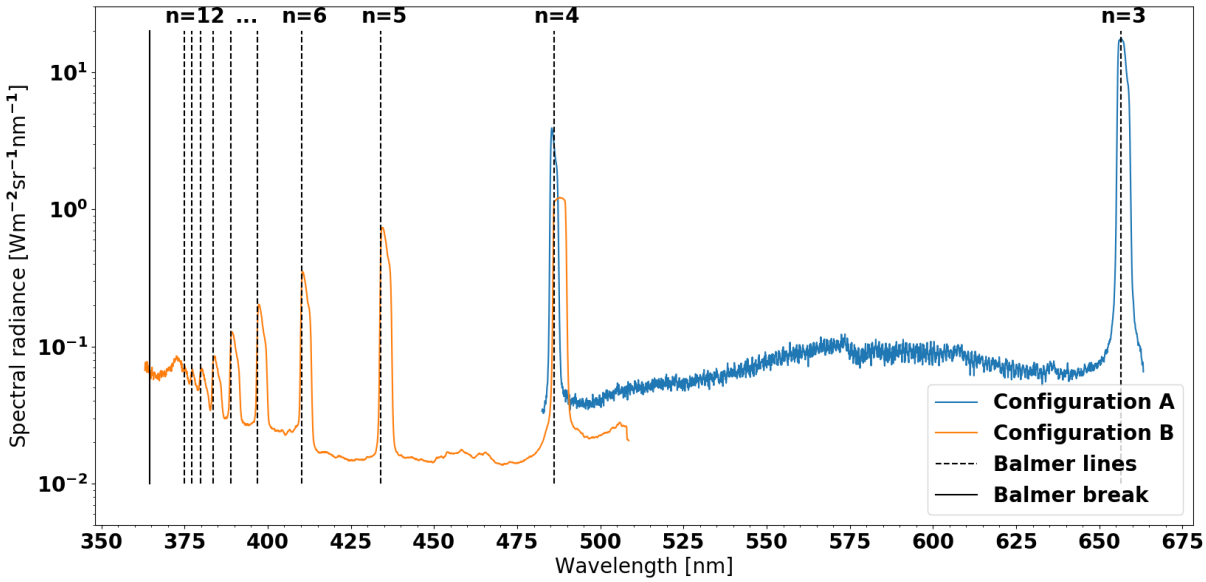

Figure 5: Example spectrum of the hydrogen plasma, in this case for a recombining plasma. The upper state excited state is indicated, the lower excited state is $n = 2$ for all the lines of interest. H_α $(n = 3 \rightarrow 2)$and H_β $(n = 4 \rightarrow 2)$ are measured using one grating angle, then H_β trough to the Balmer continuum are measured using another.

Figure 6 gives an overview of the OES results. The left graphs show radial profiles of the different excited states measured, for neutral background pressures of 0.3 Pa (no gas puffing) in the top graph, 3.5 Pa in the center graph, and 12.7 Pa in the bottom one. The right graphs are also known as 'Boltzmann plots', and show atomic state distribution functions (ASDFs) as a function of excited state energy at the same pressures. The excited state profiles are peaked in the low- and high-pressure cases, but hollow in the case of moderate neutral background pressure.

Given the geometry of Magnum-PSI, this hollow character points to the dominance of molecular reactions in producing excited hydrogen. Background neutrals are rapidly depleted as they enter the plasma beam, mainly due to heating by ion-molecule elastic collisions. A simple model suggests that these elastic collisions alone can produce a rarefication by a factor of two orders of magnitude under representative conditions [16]. The rate coefficients for dissociation, ion conversion, and dissociative attachment under these conditions are $2 \cdot 10^{-15}\ \mathrm{m^3 s^{-1}}$, $1 \cdot 10^{-15}\ \mathrm{m^3 s^{-1}}$, and $2 \cdot 10^{-16}\ \mathrm{m^3 s^{-1}}$, respectively. These also contribute to the hollowing of the molecular profile, but a total rate coefficient on the order of $10^{-14}\ \mathrm{m^3 s^{-1}}$ would be needed to fully explain the hollowing of molecular density profiles by a consumption of molecules [15]. The existence of the hollow molecular density profiles implies that any reaction involving molecules has a vanishing rate in the plasma center, and conversely, hollow emission profiles imply that molecular profiles are mainly responsible for producing excited H^*.

Further, plasma emissions are increased greatly in intensity in the 3.5 Pa case compared to the situation without hydrogen gas puffing, for example by a factor ~ 2.5 for the H_α line. These results of increased emissions and hollow emission, combined with the earlier observation of lower electron density, point to MAR as their cause. This is because MAR is a molecular process that efficiently produces excited states of hydrogen and acts as a sink for electron-ion pairs. Excited hydrogen is produced at level $n = 3$

for the negative ion-mediated branch and at levels $n = 2 - 4$ for the ion-conversion branch, and subsequently redistributed among all observed excited states by collisional (de-)excitation.

The atomic state distribution function (ASDF) plotted in the right-hand graphs of Figure 6 is given by the densities of different excited states of the hydrogen atom divided by their statistical weights, n_q/g_q where $g_q = 2q^2$. Here, q is the principal quantum number of the excited state. The ASDF is shown at three different locations: $r = 0$ is the plasma center, $r = 4.4$ mm is the location where excited state profiles are peaked in the cases where they are hollow (this location is almost independent of neutral background pressure in the intermediate range but changes with source current), and $r = 9.8$ mm is the periphery of the plasma.

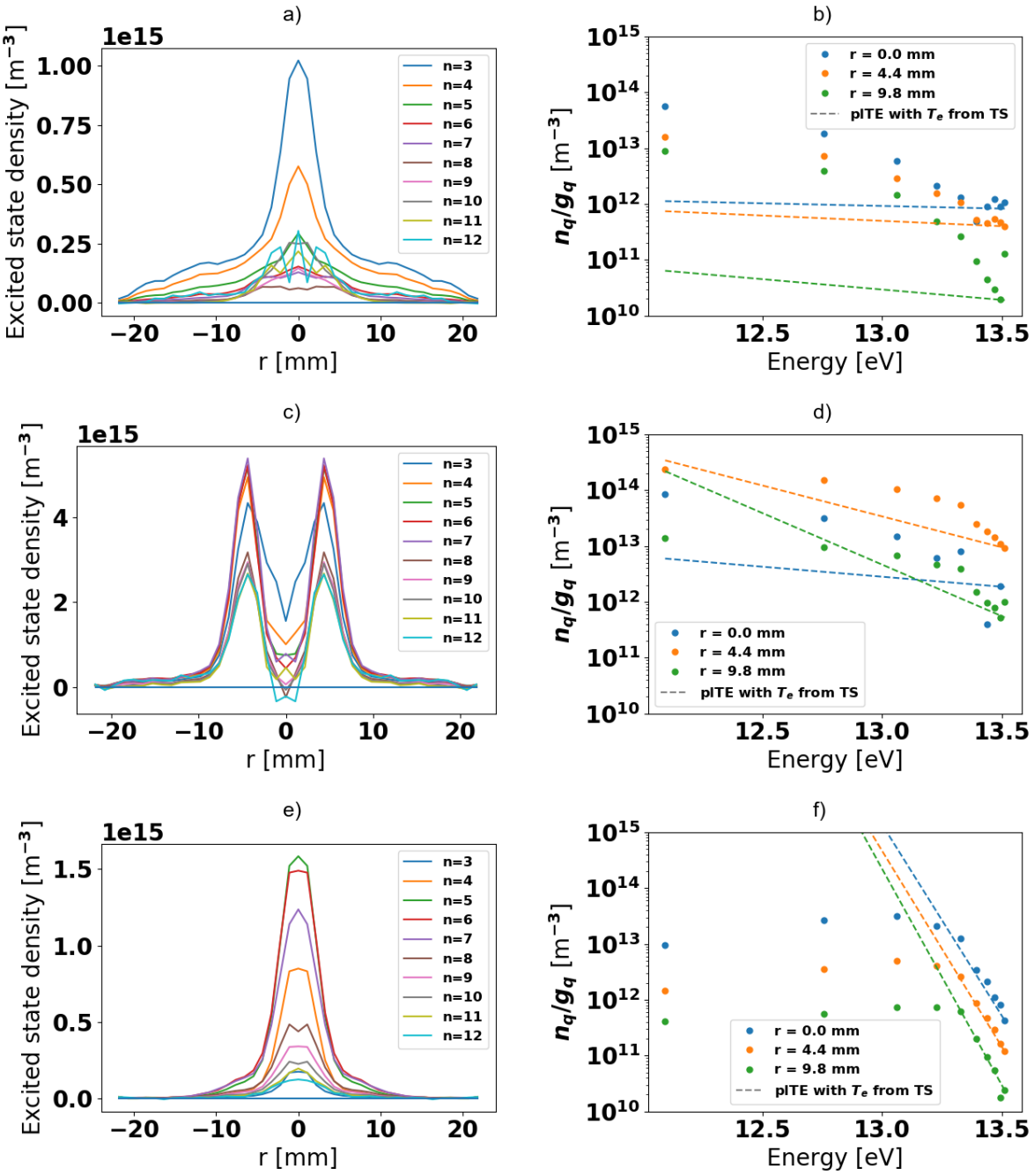

Figure 6: Profiles of excited states (a,c,e) and atomic state distribution function as a function of excited state energy - including dotted lines corresponding to a partial local thermodynamic equilibrium - at different radii (b,d,f), for neutral background pressures of 0.3 Pa (a,b), 3.5 Pa (c,d), and 12.7 Pa (e,f), all for the same plasma settings at 140 A. The hollow excited state profiles in (c) suggest a dominant molecular contribution to plasma radiation in the presence of moderate gas puffing.

In a plasma in perfect thermal equilibrium, these would follow a Boltzmann distribution and hence the points in the graph would lie on a straight line with a slope of $-\frac{1}{k_b T_e}$. Plasma-chemical processes that produce H^* can disturb this balance, however. Species like H and H^+ that have life-times much longer than that of the various states of H^* , can be transported between regions of plasma with significantly different plasma conditions. As a result, their local densities can be out of thermal equilibrium, and an abundance of ground state H can locally undergo excitation and preferentially populate lower excited states. Conversely, an abundance of H^+ can undergo EIR and preferentially populate the higher excited states [26]. MAR directly produces low excited states of hydrogen, $n = 2 - 4$ for the ion conversion branch and $n = 3$ for the negative ion-mediated branch. [7, 27] The low excited states of hydrogen are potentially under- or over-populated with respect to a Boltzmann distribution depending on which plasma processes are dominant. The higher excited states may still be in partial local thermodynamic equilibrium (plTE) with each other, due to the small energy spacing of the upper levels.

Figure 6b shows that in the low neutral pressure environment, the lower excited states are clearly overpopulated with respect to the Boltzmann distribution. This, together with the peaked emission profile, demonstrates that excitation is the main source of excited hydrogen, and indicates atomic ionization as dominant plasma process, consistent with the Thomson Scattering results. Figure 6f shows that at very high background pressure, the highly excited states are populated according to the measured electron temperature, thus, they appear in plTE with the ionic state according to the Saha equation. The lower excited states are clearly underpopulated with respect to a single Boltzmann distribution, in fact the $n = 4$ and $n = 5$ excited states exhibit population inversion with respect to $n = 3$. Together with the peaked emission profiles, this confirms EIR as the primary source of excited hydrogen, and the most important plasma process in these conditions. In literature, population inversion of the $n = 4, 5,$ and 6 excited states has previously been observed in plasmas dominated by three-body recombination [28].

In the 3.5 Pa case, the ASDF at $r = 0$ is dominated by noise for the higher excited states, since the Abel-inverted emission profiles approach and even spuriously fall below 0. Amplification of noise in the center of profiles is a normal feature of the Abel transform, since only the central line of sight contains *any* information about the center, and this is averaged with off-center information [29]. Still, the lower excited states are overpopulated within error margins, which is consistent with excitation playing a major role in the center, where molecules are depleted. At $r = 4.4$ mm, where the excited state profiles reach their maximum, there is moderate overpopulation of the lower excited states, consistent with production of intermediate excited states by MAR. At $r = 9.8$ mm, the $n = 3$ excited state (and only that state) is underpopulated with respect to Boltzmann, suggesting that at the periphery of the plasma, EIR starts to dominate.

Molecular spectroscopy

In order to gain more insight in the MAR processes active in the Magnum-PSI plasma, Fulcher-α band spectroscopy on hydrogen molecules is used. This technique probes the ro-vibrational distribution of hydrogen molecules in the plasma beam as described e,g, in [30]. Vibrational excitation of H_2 in particular greatly enhances the rates of the precursor reaction in both of the MAR reaction chains.

The Fulcher band consists of emission lines resulting from relaxation of excited molecules from the $d^3\Pi_u$ state to the $a^3\Sigma_g^+$ state. The level of vibrational (denoted by quantum number v) and rotational (denoted by quantum number K) excitation in both states determines the precise energy difference and hence the corresponding wavelength of the Fulcher band lines. The energy G of the molecular state depends on v and K as:

$$G(v,K) = T_{el} + \omega_e\left(v+\frac{1}{2}\right) - \omega_e x_e\left(v+\frac{1}{2}\right)^2 + \left(B_e - \alpha_e\left(v+\frac{1}{2}\right)\right)K(K+1), \quad (5)$$

where T_{el} indicates the electronic energy level, and the molecular constants ω_e, $\omega_e\chi_e$, B_e, and α_e are first and second order terms in a vibrating rotator model of the molecule [31]. These constants depend on the electronic state and are tabulated in the NIST database [32].

An example of a Fulcher band spectrum measured in Magnum-PSI is shown in Figure 7, for the same 140 A settings without gas puff discussed in the previous section. In these measurements, a higher-resolution diffraction grating with 2400 ln/mm is used. Three recordings at different grating angles are used to cover all the Q-branch lines of the main diagonal transitions with $\Delta v = 0$ between $602-625$nm. The instrument function is a gaussian with a FWHM of 67 pm. The Q-branch lines are identified in Figure 7, and their theoretical wavelengths in vacuum [33] are given by the vertical lines.

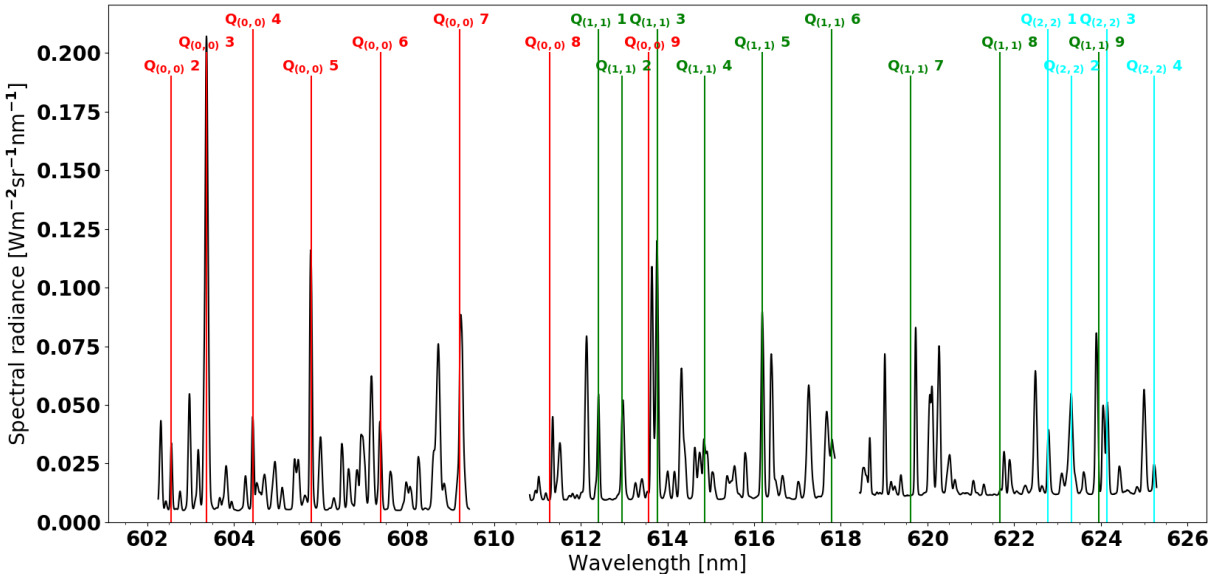

Figure 7: Example Fulcher band measurement. Vertical lines are theoretical predictions for wavelength, which match well with the experimentally identified lines.

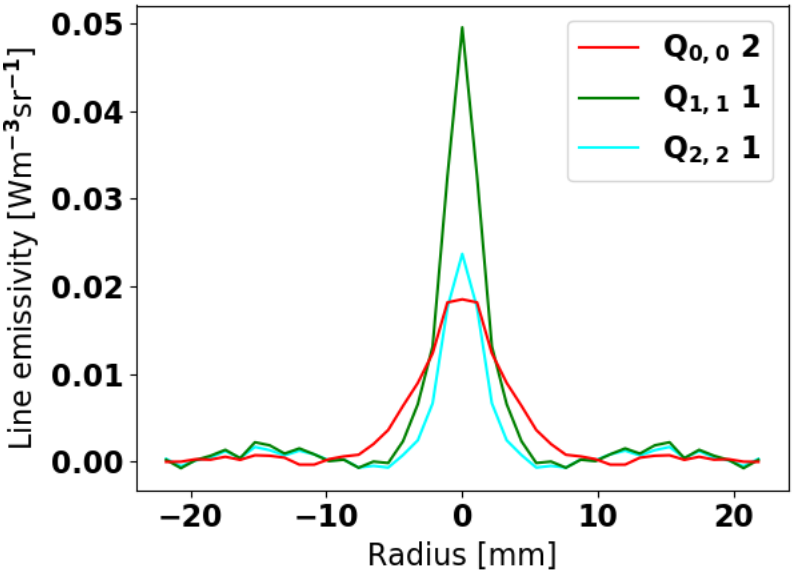

Figure 8: Radially resolved line intensities for selected Q-branch lines of the Fulcher band for a 140 A plasma at a background pressure of 3.5 Pa. Unlike the Balmer emission profiles which are fully hollow in this scenario, the Q-branch lines are peaked in the center of the plasma, for each ro-vibrational state.

The intensities of the identified Q-branch lines are fitted with a Gaussian function and a numerical Abel inversion is performed. The resulting radially resolved line intensities of the lowest observed rotational level for each observed vibrational state are presented in Figure 8, for a source current of 140 A and neutral background pressure of 3.5 Pa. Strikingly, the Q-branch line emissions are peaked in the center of the plasma, unlike the Balmer line emissions which were shown in Figure 6c to have hollow shapes in this plasma scenario. This peaked profile shape persists for all observed molecular lines and for all machine settings investigated. It may be that for the $a^3\Sigma_g^+$ state, the higher excitation rates due to higher T_e in the center of the beam outweigh the effect of depletion of molecules in the electronic ground state.

We quantitively estimate the effect of molecular excitation for the 3.5 Pa scenario shown in Figure 6c and Figure 8. The molecular emission have Half-Width at Half-Maximum (HWHM) of $2-3$ mm. T_e equals 1.2 eV at $r=0$ and 0.7 eV at $r=3$ mm. Assuming that the excitation rate scales as $\exp\left(-\frac{E_{a^3\Sigma_g^+}}{k_B T_e}\right)$ with $E_{a^3\Sigma_g^+} = 13.8$ eV the energy level of the upper Fulcher state, the excitation rate varies by a factor of more than 3 orders of magnitude. It is hence possibly consistent that a rarefication of molecules by one or two orders of magnitude causes hollow molecular density and atomic emission profiles, without causing hollow molecular emission profiles.

When the rotational distribution within a vibrational state is in a Boltzmann equilibrium, the rotational populations and hence line intensities are given as [34]:

$$I(K) \propto (2K+1)(2\Gamma+1)e^{\left(-\frac{G}{k_b T_{rot}}\right)}, \tag{6}$$

where Γ is the total nuclear spin; $\Gamma = 0$ for the para-state (K even) and $\Gamma = 1$ for the ortho-state (K odd).

The fitted Q-branch intensities per vibrational level, normalized by their statistical weights $(2K+1)(2\Gamma+1)$, are fitted to this Boltzmann distribution to find the rotational temperatures.

Figure 9 shows an example fit for the central sightline of the 140 A plasma with no gas puffing. Not all rotational levels are used in the fits. Q(0,0)3, Q(1,1)2 and Q(1,1)3 are known from literature [16,35] to

overlap spectrally with other Fulcher band lines. Moreover, Q(1,1)9 and Q(2,2)2 consistently produce higher intensities than expected in this work, which is also likely caused by overlapping lines. These 5 lines are ignored in this analysis, and the corresponding points are marked with crosses in Figure 9. The fits show that rotational temperature increases with vibrational state, a result which is not uncommon in literature [30,36,37].

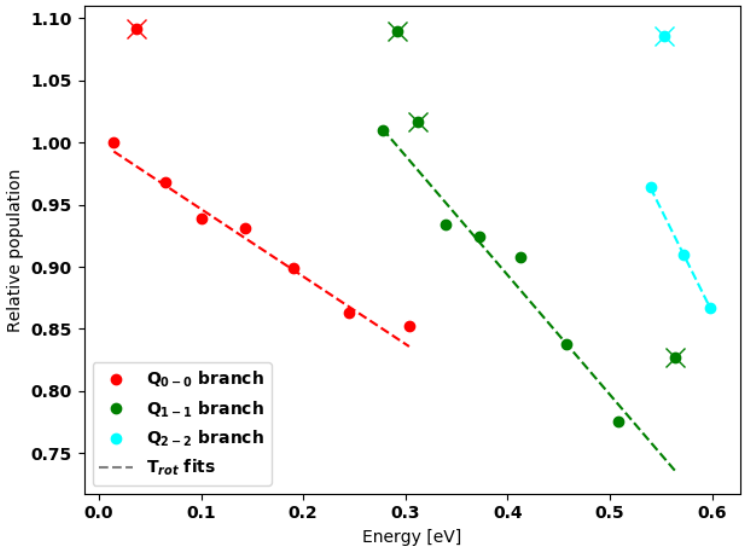

Figure 9: Rotational distribution for the different vibrational states of the 140 A plasma without gas puff, as a function of the ro-vibrational energy of each state. The higher excited vibrational states show steeper slopes and hence lower rotational temperature; fitted rotational temperatures are $(2.7 \pm 0.4) \cdot 10^3$ K, $(1.5 \pm 0.3) \cdot 10^3$ K, and (887 ± 4) K, for the vibrational levels 0, 1, and 2, respectively. The crosses indicate points not used in the fit; the relevant line intensities are anomalously high due to overlap with other spectral lines.

The vibrational distribution of the $d^3\Pi_u$ state is described by assuming Franck-Condon excitation of molecules from the electronic ground state $X^1\Sigma_g^+$ to the upper Fulcher state. For these ground state molecules, the vibrational distribution $f(v_0)$ is assumed to be in Boltzmann equilibrium with vibrational temperature $T_{vib,0}$. The Franck-Condon factors for the ground state vibrational levels v_0 are weighted by a factor $e^{\frac{E(v_0)}{k_B T_e}}$ to account for the reduction in threshold energy for excitation due to vibrational excitation [38]. Rotational distributions, vibrational redistribution in the $d^3\Pi_u$ state, and electronic excitation from levels other than the ground state are neglected. This leads to the following expression for $f(v')$:

$$f(v') \propto \sum_{v_0} q_{v'v_0}\, e^{\frac{E(v_0)}{k_b T_e}}\, e^{-\frac{E(v_0)}{k_b T_{vib,0}}}. \tag{7}$$

Experimentally, $f(v')$ is determined by the total radiated intensity per vibrational state, divided by their respective branching ratios [38]. T_{vib} in the electronic ground state is then taken as a free parameter, and the theoretical distribution is fitted to the experimental.

The results for the central line of sight of the 140 A plasma, for different levels of gas puffing, are shown in Figure 10. The model fits the vibrational distribution measured at 8 Pa well, which is typical for neutral pressures of 6 Pa and higher. However, the model clearly fails for the lower pressures. The measured relative populations $f(v' = 1)$ and $f(v' = 2)$ fall below the possible model range in all experimental conditions with $p_{neut} < 6$ Pa, and hence the model distribution cannot be fitted to the experimental in these cases.

The range of possible model predictions is limited by the model's assumptions of Franck-Condon excitation from a single Boltzmann-distributed state. Note that the exponentials in (7) can be rewritten as $e^{\frac{E(v_0)}{k_b T_e}} e^{-\frac{E(v_0)}{k_b T_{vib,0}}} = e^{-\frac{E(v_0)}{k_b}\left(\frac{1}{T_{vib,0}} - \frac{1}{T_e}\right)}$, meaning that the correction for vibrational excitation has no impact on the range of possible distributions that the model can output, but only shifts which vibrational temperature corresponds to which distribution. Due to the structure of the Franck-Condon coefficients and the Boltzmann distribution, the predicted relative populations of $v' = 1$ and $v' = 2$ reach a minimum at combinations where $\left(\frac{1}{T_{vib,0}} - \frac{1}{T_e}\right)^{-1} = 1.14 \cdot 10^4$ K, for example $T_{vib,0} = 1.14 \cdot 10^4$ K and $T_e = \infty$ (which corresponds to dropping the correction for enhanced electronic excitation due to vibrational excitation), or lower $T_{vib,0}$ at finite T_e.

A likely source of model mismatch is the neglect of the rotational distribution of the molecular ground state. This distribution may exhibit a two-temperature distribution with a higher temperature for the higher rotational states [39]. The highly excited rotational states couple more effectively to the $v' = 0$ state, and may cause the observed distribution to fall out of the fit bounds [40]. To verify and correct for such an effect, Fulcher band measurements should be taken between 600-640 nm with a spectral resolution of 0.02 nm or better in order to cover and resolve also the high rotational levels [39].

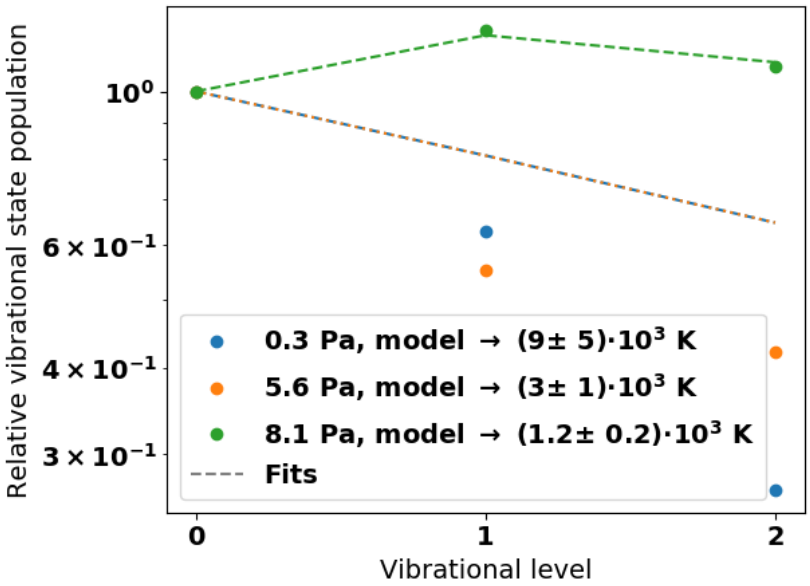

Figure 10: Measured vibrational distribution of the $d^3\Pi_u$ state for a plasma with 140 A source current at different neutral pressures, and fitted distributions corresponding to vibrationally-enhanced Franck-Condon excitation of ground-state molecules in a Boltzmann distribution. The model fails to describe the measured distribution at the lower pressures, with the data falling significantly below the lowest possible model prediction.

Vibrational and rotational temperatures for the entire background pressure scan of the 140 A plasma setting are summarized in Figure 11. At pressures below 6 Pa, the analysis of the vibrational distribution fails and no vibrational temperature is found. T_{rot} of each vibrational state shows an increase with neutral pressure at low gas puff levels and a decrease at higher levels of gas puff. At the higher pressures, T_{vib} shows a similar decrease with p_{neut}. The eventual decrease can be understood by a decrease in T_e; there is less energy available to transfer to the molecules. The initial increase may be due to higher neutral pressures causing a decrease in the neutral diffusion coefficient. This would increase the residence time of the molecules, allowing for more excitation before they are expelled from the plasma.

In the high-pressure cases, the extracted $T_{vib,0}$ allows an estimate of the rates of both ion-conversion MAR and negative-ion mediated MAR in the Magnum-PSI plasma. At lower pressures – which are of greater interest since Balmer line spectroscopy indicates a larger role for MAR there – an estimate is given based on the assumption that the vibrational temperature is larger than the measured rotational temperature of the Q(0,0) branch by a factor 1-2. The vibrationally resolved rate coefficients of the precursor steps in reactions (1) and (2), compiled by Reiter et al. [41], are combined with a Boltzmann distribution for the vibrational states to yield the precursor reaction rate coefficients.

The fraction of H_2^+ or H^- ions that actually lead to recombination is calculated by accounting for (i) the probability that the produced excited state is re-ionized and (ii) the probability that H_2^+ undergoes dissociation or dissociative ionization instead of dissociative recombination (proton impact electron detachment of H^- is neglected). These probabilities are calculated as quotients of the relevant rate coefficients from another work by Reiter et al. [42]. This yields the effective rate coefficients of both types of MAR. Effective rate coefficients of ionization and EIR are taken directly from ADAS [11].

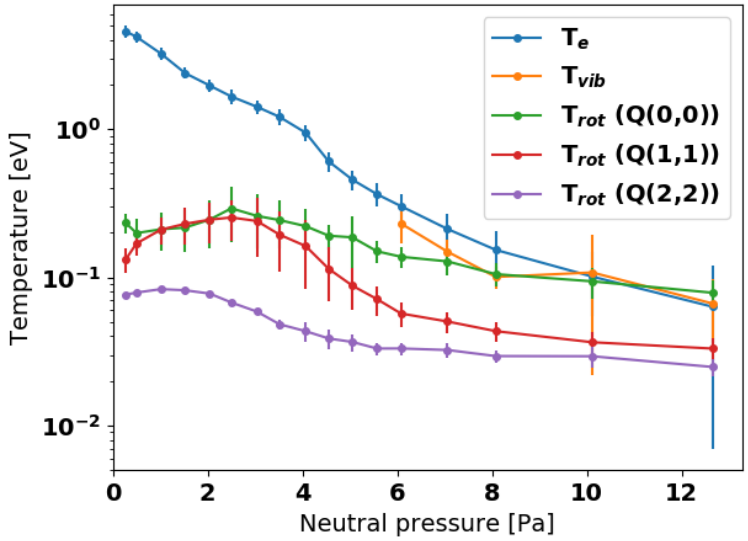

Figure 11: Rotational temperatures of the upper Fulcher state and vibrational temperatures of the molecular ground state, determined from Fulcher band emissions, compared to peak electron temperature as a function of background pressure for the 140 A plasma. For neutral pressures below 6 Pa, the Boltzmann/Franck-Condon model fails and no well-defined vibrational temperature can be extracted from the data.

To convert rate coefficients to rates, we assume the neutral density is given from the neutral pressure by the ideal gas law at room temperature, assuming a dissociation degree of 50%. Rarefaction of the neutrals in the plasma beam is ignored, which results in an overestimate for MAR and ionization. Central values of T_e and n_e are used. The resulting rates of ionization, EIR, and both types of MAR are plotted in Figure 12 as function of neutral background pressure for the 140 A plasma. In the case of MAR, the rates are calculated assuming $T_{vib,0}$ is a factor 1 to 2 higher than te T_{rot} measured from the

Q(0,0) branch. These results confirm that for increasing neutral pressure, ionization, MAR, and EIR dominate in turn. Whether negative-ion mediated MAR is relevant depends strongly on the assumptions on the vibrational temperature; its rate is only a factor 2-3 smaller compared to ion conversion MAR when assuming $T_{vib,0} = 2T_{rot,Q(0,0)}$, but smaller by more than an order of magnitude if equality of the temperatures is assumed.

At a neutral pressure of 3.5 Pa, the factor between the MAR rate and the atomic reaction rates reaches its maximum. The effective rate coefficient for ion-conversion MAR at this pressure is $1 - 4 \cdot 10^{-18}$ $\mathrm{m^3 s^{-1}}$, depending on the assumptions for T_{vib}. The rate is enhanced by up to a factor 6 due to vibrational excitation of the molecules (compared to a case where all hydrogen molecules are in the vibrational ground state). In the same conditions, negative-ion mediated MAR has an effective rate coefficient of $3 \cdot 10^{-19} - 2 \cdot 10^{-17}$ $\mathrm{m^3 s^{-1}}$, with vibrational excitation responsible for an enhancement of up to three orders of magnitude. The overestimate for molecule density yields a total effective MAR reaction rate of $4 \cdot 10^{23} - 3 \cdot 10^{24}$ $\mathrm{m^{-3} s^{-1}}$. Assuming constant conditions over the 0.38 m that the plasma traverses in the target chamber, the particle flux reduction due to MAR is given as the product of reaction rate and distance: $2 \cdot 10^{23} - 1 \cdot 10^{24}$ $\mathrm{m^{-2} s^{-1}}$. Comparing these numbers to the original particle flux of $2 \cdot 10^{24}$ $\mathrm{m^{-2} s^{-1}}$, the possible relevance of MAR as a recombination pathway hence depends on what vibrational temperatures are actually produced and how strongly the molecules are rarefied in the plasma beam.

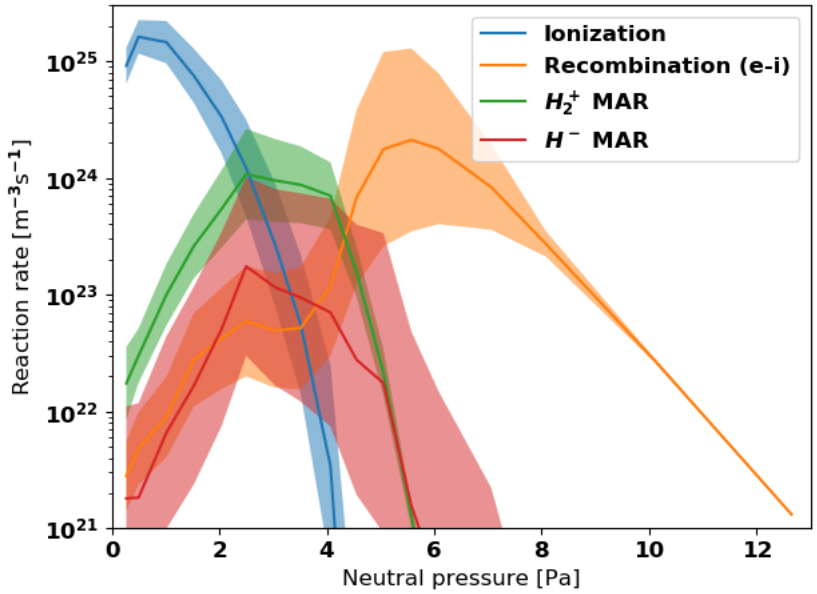

Figure 12: Rates of relevant atomic and molecular processes in the Magnum-PSI plasma as a function of neutral background pressure. Ion-conversion MAR has a higher reaction rate than ionization and EIR in a narrow range around 3.5 Pa. The degree to which MAR dominates, and whether negative ions play a significant role, depends sensitively on the assumptions for vibrational temperature. The error margins are only due to measurement uncertainties for ionization and recombination, but dominated by the assumption that $T_{rot} < T_{vib} < 2T_{rot}$ for the MAR branches.

Discussion and conclusions

Hydrogen gas puffing was introduced in the last of the three differentially-pumped vacuum chambers of Magnum-PSI. The evolution of plasma kinetic parameters, the shape of Balmer line emission profiles, and the relative populations of hydrogen excited states all indicate that as the level of gas puff is increased, the plasma passes through regimes where ionisation, MAR, and atomic recombination dominate in turn. For the highest levels of gas puff, target heat flux, electron temperature and electron

density were all reduced to below the detection limit of the Thomson Scattering system. Extrapolating this result to a tokamak geometry makes it likely that local gas puffing in the divertor region can mitigate downstream plasma conditions from typical Magnum-PSI values ($\sim 5\,\mathrm{eV}, 1\cdot 10^{20}\,\mathrm{m}^{-3}$, $2\cdot 10^{24}\mathrm{m}^{-2}\mathrm{s}^{-1}$, $10\,\frac{\mathrm{MW}}{\mathrm{m}^2}$) to negligible. Such values are comparable to the ITER semi-detached divertor. Whether more extreme plasma loading could be mitigated effectively remains unclear. Also, the possible deterioration of upstream plasma conditions due to escaping neutrals cannot be addressed by this work. However, such an effect may be limited in divertor designs with a large degree of closure [43, 44, 45].

Fulcher band spectroscopy indicates that indeed, the MAR rate exceeds those of ionization and EIR in the moderate pressure regime. How the MAR rate compares to the incoming particle flux or whether there is a role for negative ions cannot be answered by our measurements, since the vibrational distribution of the molecular $d^3\Pi_u$ state observed in Fulcher band spectroscopy fell outside the possible range used in the model. This model was based on the assumptions of a molecular ground state in Boltzmann equilibrium, excitation to the $d^3\Pi_u$ state according to Franck-Condon factors, and no excitation from other vibrational states or vibrational redistribution during the lifetime of the $d^3\Pi_u$ state. The most likely explanation is a lack of thermal equilibrium in the rotational distribution of the molecular ground state. This issue can be addressed by repeating the measurements at higher spectral resolution and coverage in order to incorporate more rotational levels of the $d^3\Pi_u$, which can better constrain the ground-state ro-vibrational distribution. Alternative, an active laser diagnostic such as VUV-LIF can be used to more directly probe the molecular ground state.

Another point of interest is that the Fulcher band line intensities do not show any hollow profile as was observed for the Balmer lines. This may be explained by the T_e-dependence of excitation of molecules to the upper Fulcher state if rarefaction of the molecules is limited.

In short, the role of hydrogen molecular effects on detachment in Magnum-PSI is to provide a significant particle sink, which contributes to reduced electron densities and target heat loads. In the most favorable conditions for MAR, achieved with neutral pressures of 3-4 Pa, MAR is the main recombination mechanism, and outweighs ionization to produce a net particle sink.

The results presented in this work serve as a benchmark for modelling suites that aim to simulate the ITER divertor, and motivates their accurate treatment of the discussed processes, particularly MAR. The wide range of conditions studied, where the processes of ionisation, MAR, and EIR in turn take on a dominant role, provide a framework where the implementation of each of these can be validated in detail.

As noted before, isotope effects, such as differences in vibrational structure, cause differences in the MAR rates between isotopes. For example, direct measurements of the dissociative attachment rate show that the process is strongly reduced in D_2 compared to H_2 [46], resulting in a lower rate of D^--mediated MAR compared to H^--mediated MAR. Chiefly, this means that our results regarding the relative importance of the two MAR reactions are not necessarily valid for D-T plasmas as in the ITER divertor. More experiments in Magnum-PSI in D plasma can extend the explicit validation range of transport codes to deuterium. For tritium, corrections must be made from the perspectives of theory and scattering simulations.

Bibliography

[1] D.M. Duffy, Phil. Trans. R. Soc. A, Vol. 368 (2010).
[2] A. Kallenbach, M. Bernert, M. Beurskens, L. Casali, M. Dunne, T. Eich, L. Giannone, A. Herrmann, M. Maraschek, S. Potzel, Nucl. Fusion 55 (2015) 053026 (8pp)
[3] J.R. Harrison, W.A.J. Vijvers, C. Theiler, B.P. Duval, S. Elmore, B. Labit, B. Lipschultz, S.H.M. van Limpt, S.W. Lisgo, C.K. Tsui, et al., *Detachment evolution on the TCV tokamak*, Nuclear Materials and Energy (2016)
[4] B. Lomanowski, M. Carr, A. Field, M. Groth, A. E. Jaervinen, C. Lowry, A. G. Meigs, S. Menmuir, M. O'Mullane, M. L. Reinke et al., Nuclear Materials and Energy 20 (2019) 100676
[5] A.L. Moser, A.W. Leonard, A. G. McLean, H. Q. Wang, J. G. Watkins, Nuclear Materials and Energy 19 (2019) 67–71
[6] S.I. Krasheninnikov & A.S. Kukushkin, *Physics of ultimate detachment of a tokamak divertor plasma*, J. Plasma Phys. (2017), vol. 83, 155830501
[7] R.K. Janev, D. Reiter, U. Samm, *Collision processes in low-temperature hydrogen plasmas*, Berichte des Forschungszentrums Jülich, Vol. 4105, (2003).
[8] M. Sakamoto, A. Terakado, K. Nojiri, N. Ezumi, Y. Nakashima, K. Sawada, K. Ichimura, M. Fukumoto, K. Oki, K. Shimizu, N. Ohno et al., Nuclear Materials and Energy 12 (2017) 1004.
[9] R. Perillo, R. Chandra, G.R.A. Akkermans, I.G.J. Classen, S.Q. Korving, Phys. Plasmas, 26(10):102502 (2019)
[10] A.S. Kukushkin, S.I. Krasheninnikov, A.A. Pshenov, D. Reiter, *Role of molecular effects in divertor plasma recombination*, Nucl. Mater. Energy (2017).
[11] The iso-nuclear master files from the ADF11 class on the open version of the atomic data and analysis structure, http://open.adas.ac.uk/, version 2.0, OPEN-ADAS .
[12] M.J. de Graaf, R. Severens, R.P. Dahiya, M.C.M. van der Sanden, D. Schram, Phys. Rev. E, vol. 48, no. 3, pp. 2098–2102, 1993.
[13] N. Ohno, N. Ezumi, S. Takamura, S. I. Krasheninnikov, A.Yu.. Pigarov., Phys. Rev. Lett. 81, Phys. Rev. Lett., vol. 81, pp. 818–821, 1998.
[14] N. Ezumi, D. Nishijima, H. Kojima, N. Ohno, S. Takamura, S.I. Krasheninnikov, A.Yu. Pigarov, J. Nucl. Mater., vol. 269, pp. 337–342, 1999.
[15] A.E. Shumack, V.P. Veremiyenko, D.C. Schram, H.J. de Blank, W.J. Goedheer, H.J. van der Meiden,W.A.J. Vijvers, J. Westerhout,N.J. Lopes Cardozo, G.J. van Rooij, Phys. Rev. E, 78(4), 046405 (2008).
[16] N. Den Harder, D.C. Schram, W.J. Goedheer, H.J. De Blank, M.C.M. Van de Sanden, G.J. Van Rooij., Plasma Sources Sci. Technol. 24 025020, 2015.
[17] S. Wiesen, D. Reiter, V. Kotov, M. Baelmans, W. Dekeyser, A.S. Kukushkin, S.W. Lisgo, R.A. Pitts, V. Rozhansky, G. Saibene et al., J. Nucl. Mater., vol. 463, pp. 480–484, 2015.
[18] R. C. Wieggers, P. W. C. Groen, H. J. de Blank, W. J. Goedheer, Contrib. to Plasma Phys., vol. 52, no. 5–6, pp. 440–444, 2012.
[19] H.J.N. van Eck, G.R.A. Akkermans, S. Alonso van der Westen, D.U.B. Aussems, M. van Berkel, S. Brons, I.G.J. Classen, H.J. van der Meiden, T.W. Morgan, M.J. van de Pol, et al., *High-fluence and high-flux performance characteristics of the superconducting Magnum-PSI linear plasma facility,* Fusion Engineering and Design, 142, 26-32 (2019).
[20] N. Ohno, *Plasma Detachment in Linear Devices*, Plasma Phys. Control. Fusion 59 (2017) 034007 (9pp).
[21] R.A. Pitts, X. Bonnin, F. Escourbiac, H. Frerichs, J.P. Gunn, T. Hirai, A.S. Kukushkin, E. Kaveeva, M.A. Miller, D. Moulton et al., Nucl. Mater. Energy 20 (2019) 100696.
[22] H.J. van der Meiden, A.R. Lof, M.A. van den Berg, S. Brons, A.J.H. Donné, H.J.N. van Eck, Peter Koelman, W.R. Koppers, O.G. Kruijt, N.N. Naumenko, et al., Rev. Sci. Instrum. 83 (2012) 123505, https://doi.org/10.1063/1.4768527.
[23] P.C. Stangeby, *The Plasma Boundary of Magnetic Fusion Devices*, Taylor & Francis Group, 2000.
[24] T.W. Morgan, M.A. van den Berg, G. De Temmerman, S. Bardin, D.U.B. Aussems, R.A. Pitts, Nucl. Fusion **57** (2017).
[25] C. J. Dasch, Appl. Opt. 31, 1146–1152 (1992).

[26] J. A. M. van der Mullen, *Excitation equilibria in plasmas; a classification*, Physics Reports Vol. 191, pp 109-220, 1990.
[27] W. E. N. van Harskamp, C. M. Brouwer, D. C. Schram, M. C. M. van de Sanden, R. Engeln, Phys. Rev. E 83 (2011) 036412.
[28] K. Shibagaki & K. Sasaki, J. Phys. D: Appl. Phys. 41 (2008) 195204.
[29] A. T. Ramsey & M. Diesso., Rev. Sci. Instrum., Vol. 70, No. 1, 1999.
[30] S. Brezinsek, P.T. Greenland, Ph Mertens, A. Pospieszczyk, D. Reiter, U. Samm, B. Schweer, G. Sergienko, J. Nuc Mater., 313–316 (2003) 967–971.
[31] G. Herzberg*, Molecular spectra and molecular structure*, Vol. I. (Krieger publishing company, 1989).
[32] NIST, *Database of Diatomic Molecules: Hydrogen*, http://webbook.nist.gov/cgi/cbook.cgi?ID=C1333740&Units=SI&Mask=1E9F (1976), [Online; accessed 27-December-2019].
[33] G.H. Dieke, *The Molecular Spectrum of Hydrogen and Its Isotopes* J. Mol. Spectrosc., Vol. 2 (1958)
[34] L. Tomasini, A. Rousseau, G. Gousset, P. Leprince et al., J. Phys. D: Appl. Phys. Vol 29, No. 4, 1996.
[35] H. M. Crosswhite, *The hydrogen molecule wavelength tables of Gerhard Heinrich Dieke* (Wiley-Interscience, 1972).
[36] B. Heger, U.Fantz, K.Behringer, ASDEX Upgrade Team, Journal of Nuclear Materials 290-293, 413 (2001).
[37] U. Fantz, Contributions to Plasma Physics 42, 675 (2002).
[38] U. Fantz & B. Heger., Plasma Phys. Control. Fusion 40 (1998) 2023–2032.
[39] S. Briefi & U. Fantz, J. Quant. Spectrosc. Ra. 187 (2017) 135–144
[40] S. Briefi, D. Rauner, U. Fantz, Submitted to: Plasma Sources Sci. Technol., 2020
[41] D. Reiter, *The data file H2VIBR: Additional Molecular Data for EIRENE: vibrationally resolved H2* (2005).
[42] D. Reiter, *The data file AMJUEL: Additional Atomic and Molecular Data for EIRENE* (2005)
[43] W.L. Barr & B.G. Logan, Fus. Tech., 18:2, 251-256 (1990)
[44] H.Y. Guo, C.F. Sang, P.C. Stangeby, L.L. Lao, T.S. Taylor, D.M. Thomas, Nucl. Fusion 57 (2017) 044001 (5pp)
[45] H.Y. Guo, H.Q. Wang, J.G. Watkins, L. Casali, B. Covele, A.L. Moser, T. Osborne, C.M. Samuell, M.W. Shafer, P.C. Stangeby , D.M. Thomas, J. Boedo , R.J. Buttery, R. Groebner, D.N. Hill, L. Holland, A.W. Hyatt, A.E. Jaervinen, A. Kellman, L.L. Lao, et al., Nucl. Fusion 59 (2019) 086054 (13pp).
[46] E. Krishnakumar, S. Denifl, I. Cadez, S. Markelj, N. J. Mason, Phys. Rev. Lett. 106, p. 243201 (2011)

Acknowledgements

We acknowledge the support of the Magnum-PSI Facility Team at DIFFER. The Magnum-PSI facility at DIFFER has been funded by the Netherlands Organisation for Scientific Research (NWO) and EURATOM.

This work has been carried out within the framework of the EUROfusion Consortium and has received funding from the Euratom research and training programme 2014-2018 and 2019-2020 under grant agreement No 633053. The views and opinions expressed herein do not necessarily reflect those of the European Commission.

The data that support the findings of this study are available from the corresponding author upon reasonable request.